

Boise State University

ScholarWorks

Mechanical and Biomedical Engineering Faculty
Publications and Presentations

Department of Mechanical and Biomedical
Engineering

8-2021

Effect of Temperature on Abrasion Erosion in Particle Based Concentrating Solar Powerplants

Nipun Goel

Boise State University

Tessa Mei-Lin Fong

Boise State University

John P. Shingledecker

Electric Power Research Institute

Andrew Russell

Boise State University

Michael W. Keller

University of Tulsa

See next page for additional authors

Publication Information

Goel, Nipun; Fong, Tessa Mei-Lin; Shingledecker, John P.; Russell, Andrew; Keller, Michael W.; Shirazi, Siamack A.; and Otanicar, Todd. (2021). "Effect of Temperature on Abrasion Erosion in Particle Based Concentrating Solar Powerplants". *Solar Energy*, 224, 1127-1135. <https://doi.org/10.1016/j.solener.2021.06.080>

This is an author-produced, peer-reviewed version of this article. © 2021, Elsevier. Licensed under the Creative Commons Attribution-NonCommercial-No Derivative Works 4.0 International license. The final, definitive version of this document can be found online at *Solar Energy*, <https://doi.org/10.1016/j.solener.2021.06.080>

Authors

Nipun Goel, Tessa Mei-Lin Fong, John P. Shingledecker, Andrew Russell, Michael W. Keller, Siamack A. Shirazi, and Todd Otanicar

Effect of Temperature on Abrasion Erosion in Particle Based Concentrating Solar Powerplants

Nipun Goel*

Department of Mechanical and Biomedical
Engineering
Boise State University
nipungoel@boisestate.edu

Tessa Mei-Lin Fong

Department of Mechanical and Biomedical
Engineering
Boise State University

John P. Shingledecker

Electric Power Research Institute
Charlotte, NC

Andrew Russell

Department of Mechanical and Biomedical
Engineering
Boise State University

Michael W. Keller

Department of Mechanical Engineering
The University of Tulsa
and
Erosion/Corrosion Research Center (E/CRC)
The University of Tulsa

Siamack A. Shirazi

Department of Mechanical Engineering
The University of Tulsa
and
Erosion/Corrosion Research Center (E/CRC)
The University of Tulsa

Todd Otanicar

Department of Mechanical and Biomedical Engineering
Boise State University

Abstract

The use of solid particles as a heat transfer medium is being explored for concentrated solar power plants (CSP) to increase their efficiency by achieving operating temperature greater than 700 °C. During operation, these hot particles are expected to move along the various components within the collector system, resulting in material degradation from a combination of high-temperature oxidation and erosion. In the present study, the performance of candidate materials was evaluated through a series of abrasion erosion experiments at room temperature as well as at 800 °C. Wear in metallic and refractory type materials was investigated using CarboBead® HSP 40/70 particles inside a resistance heated kiln. Cross-sectional scanning electron microscopy (SEM) and energy dispersive x-ray spectroscopy (EDS) analysis on the specimens tested at 800 °C determined that the specific wear rate in Inconel 740H and stainless steel 316 metallic specimens was influenced by the thermally grown oxide morphology. High chromium Inconel 740H specimens exhibited greater resistance to wear with a steady state specific wear rate of $1.92\text{E-}4 \text{ mm}^3\text{N}^{-1}\text{m}^{-1}$ compared to $5.7\text{E-}3 \text{ mm}^3\text{N}^{-1}\text{m}^{-1}$ for Stainless Steel 316.

Keywords: concentrating solar power; abrasion erosion; solid particles,

1 Introduction

Central receivers typically utilize molten salts, gases, or liquid metal as heat transfer fluid (HTF) to absorb heat from the irradiated receiver. Irrespective of the direct or indirect receiver heat transfer methodology used, the thermal-to-electric cycle efficiencies of these plants are in the range of 30–40% with steam turbine inlet temperatures lower than 600 °C (Ho, 2017, 2016). While thermal-to-electric efficiency of the cycle increases with the increase in turbine inlet temperature, the maximum temperature achievable at turbine inlet in superheated steam systems is 550 °C whereas molten salt systems using Nitrate salts become unstable at temperatures above 600 °C (Mehos et al., 2017). Achieving high temperature not only requires design changes for process handling but also a suitable heat transfer fluid that has high reliability over thousands of thermal cycles. Particle receivers are currently being designed and tested as a means to achieve operating temperatures >700 °C. In a particle receiver, solid particles (typically sintered ceramic, or silica

sand) are used as the heat transfer medium that can be heated as they fall through a beam of concentrated sunlight for direct heat absorption. With the additional advantage that these solid particles can alternatively be heated indirectly through tube walls as well, and ease of storage in an insulated vessel, particles not only have the ability to be heated to temperatures above 1000 °C, they are also not restricted by the freezing problems at low temperatures as observed with molten salts (Flamant et al., 2013).

Different particle-based receivers that have been designed include free-falling (Siegel et al., 2010), obstructed flow (Ho et al., 2016), centrifugal/rotating kiln (Wu et al., 2015, 2014), fluidized bed (Bai et al., 2014; Flamant, 1982), and gravity driven (Ma et al., 2014; Martinek and Ma, 2015) particle receivers. Irrespective of the unique benefits associated with each particle-based receiver design, hot or cold particles will flow through discharge hoppers or along the inner receiver surfaces and other system components, depending on operating mode of the receiver. This may result in surface abrasion, impact erosion from impingement under gravitational fall, and particle attrition as particles fall and move on top of each other. Ho et al. (Ho et al., 2019) reported severe degradation in stainless steel wire mesh structures used in obstructed flow tests due to a combined effect of oxidation and surface wear, after 20 hours of testing at 700kW/m² irradiance. Solid particles have also been considered for storage media in thermal energy storage (TES) systems. Ma et al. modeled TES performance metrics in terms of three efficiencies: first-law efficiency, second-law efficiency, and storage effectiveness, to compare different available TES technologies across the board (Ma et al., 2014). They noted that the evaluated particle media such as ash, sand, refractory etc., are not only stable, abundant, and inexpensive, they also exhibited thermal self-insulation in the storage mode. This minimized thermal losses and allowed for an extended capacity to hold thermal energy for a longer period without the need of expensive metal alloys and insulation. El-Leathy et al. demonstrated that the TES systems for use with solid particles could be built with readily available materials such as insulating firebrick, perlite concrete, expansion joint, and concrete bricks, and noted that despite operation at 800 °C, the thermal energy losses were approximately 4.4% (El-Leathy et al., 2014).

The development of 3rd generation (GEN3) CSP systems will require significant technological advances in the areas of durability, while maintaining, or even enhancing, thermo-physical properties of the components operating within. A better understanding of material degradation due to erosion is necessary to ensure system durability throughout the life of CSP plant. The extent of erosion depends on many factors including but not limited to particle shape (Hutchings et al., 2017) and size (Misra and Finnie, 1981), particle hardness (Arabnejad et al., 2015), material hardness/brittleness (Oka et al., 1993; Sheldon, 1977), ductility (Finnie, 1960), particle impact velocity (Finnie and McFadden, 1978), and impact angle (Oka et al., 2005). Damage to the system components and attrition of particles results in particle loss, changes in particle morphology, and ultimately changes in thermal performance from the resulting erosion to the system. However, majority of works listed above have been done at particle velocities and temperatures that are not relevant for a GEN3 CSP systems, and therefore cannot be applied directly to evaluate performance of candidate lining materials and particles. A relatively recent work evaluated the performance of 3 different grades of steels (martensitic, ferritic, and austenitic) and nickel-based alloy 617 subject to erosion-oxidation wear. They noted clear differences in the oxide scales grown in air, but the measured mass losses at 650 °C and 750 °C were very large (experiment at 750 °C was terminated early due to high mass loss) and did not appear to be related to the oxidation resistance of the metal with the lower oxidation resistance alloy VM12 showing lower mass loss than the nickel-based alloy 617 (Galiullin et al., 2019). Although Galiullin et al. conducted the experiments at low particle to specimen relative velocities, the specimens were submerged under particles for the entire duration of the test and post-test evaluation showed significant macroscopic sample rounding and thin irregular oxide scales indicating an erosion dominated experiment. We believe that when in operation, the particle velocities will be lower and metal liner surfaces will periodically be exposed to air resulting in a potentially greater degree of oxidation exposure of the surfaces. Additionally, in the experiments conducted by Galiullin et al., the wider face of the specimen is oriented normal to the direction of motion, indicating a near 90 degrees angle of particle impact on specimen surface. As such, the erosion phenomenon could not be restricted to pure abrasion wear.

In this work, we present results from pure abrasion erosion experiments conducted at GEN3 relevant temperatures and expected particle velocities on selected candidate particles and containment materials. The durability of material was determined in terms of series of erosion exposures of selected candidate containment materials and particles. Parallel experiments conducted at room temperature were used to develop a baseline for effect of temperature on rate of material wear.

2 Experimental Procedure

2.1. Specimen Preparation

The experiments were conducted using CarboBead® HSP 40/70 particles with an average particle diameter of 285 µm due to their promising performance as the heat transfer media (Siegel et al., 2015). Three different candidate containment materials were selected from those currently being considered as the lining material in storage bins and wall materials of particle-to-sCO₂ heat exchangers. These materials were chosen upon consultation with multiple research partners and individuals who had an interest in this field, and also keeping in mind that cost will be a significant driver in the eventual choice for liner material. Of these two are metallic and the third one is a 60% alumina, low-cement refractory castable from Allied Mineral Products® (hereon afterwards referred to as fireclay cement type refractory material or simply refractory material in figures). The chemical composition of the specimens and the HSP 40/70 particles are provided in Table 1 and Table 2 respectively.

Table 1: Percentage Chemical Composition of containment materials tested for abrasion against HSP 40/70 particles.

Chemical Composition	Stainless Steel 316	Inconel 740H®	Fireclay cement Refractory material
Fe	65.6	0.2	-
Cr	17.0	24.6	-
Mo	2.5	0.5	-
Ni	12.0	50.0	-
Co	-	20.1	-
C	0.08	0.03	-
Al	-	1.39	-
Ti	-	1.45	-
Nb	-	1.47	-
Mn	2.0	0.3	-
Si	0.75	0.15	-
Al ₂ O ₃	-	-	61.3
SiO ₂	-	-	32.8
TiO ₂	-	-	2.4
CaO	-	-	1.9
Fe ₂ O ₃	-	-	1.0

Table 2: Percentage Chemical Composition of HSP 40/70 particles.

Al_2O_3	70 – 90
SiO_2	5 – 20
TiO_2	1 – 10
Fe_2O_3	5 – 20

Stainless steel alloy 316 and the nickel-based alloy Inconel® alloy 740H® were cut to size 2.54 cm in length, 1.27 cm in width and a variable thickness of 0.31 cm – 0.5 cm depending on the size of stock available as shown in Figure 1a and Figure 1b respectively. The metallic specimens were drilled and tapped for easy mounting on the rotating shaft. The materials were evaluated in their as-received state (solution annealed for the 316 and solution annealed and aged at 800 °C-4hrs for the 740H) without additional surface preparation. The fireclay cement type refractory material was cut to 2.54 cm length by 2.54 cm width and a thickness of 1.3 cm using a wet tile saw and drilled through the center using a water-cooled core drill bit (See Figure 1c). Threaded rods were inserted through these holes and held in place using nuts and washers. The drilled hole with the threaded rod was also filled with mortar to prevent particles from slipping into the empty spaces and thus prevent artificial weight gains. The specimens were then allowed to air dry for 48 hours until the mortar set completely.

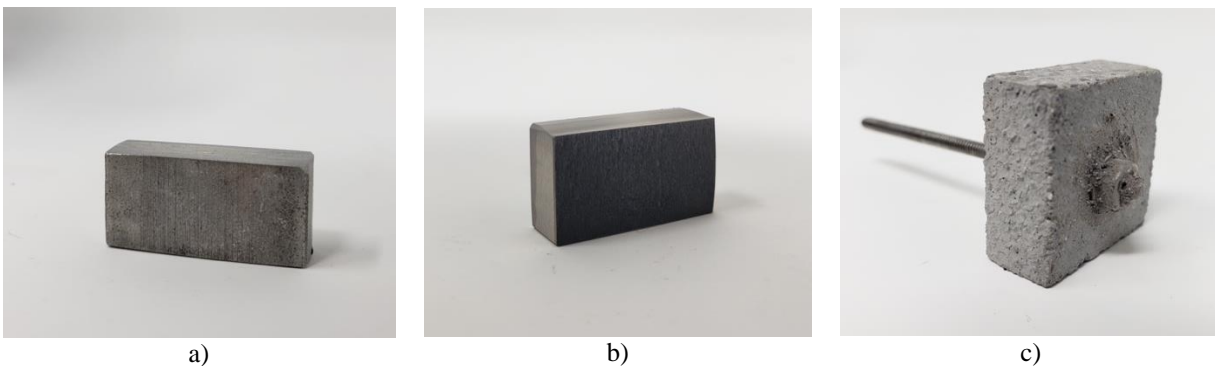


Figure 1: Prepared specimens of a) SS316, b) Inconel 740H, and c) fireclay cement type refractory materials

2.2. Abrasion Testing

Abrasive wear is defined as the damage to surface due to a relative sliding motion of a second surface on it. For particle receiver systems, such wear is expected in lining materials from the sliding movement of hot or cold particles along the surface of lining material. To measure abrasion erosion in CSP systems, an experimental setup based on the impeller-tumbler method of testing abrasion was developed to enable testing at the unique operating conditions expected in a particle receiver CSP plant. Figure 2 shows the schematic of the abrasion setup. Specimens are mounted onto a rotating shaft and continuously rotated through a bed of particles placed inside a trough. This setup allows for operation at the low speed dense granular flow conditions expected in the storage tanks during discharge and through the heat exchangers. The system design also ensures a near zero angle of contact between the particles and with low rotation speeds, any wear from particle impact is near negligible and pure abrasion wear is observed.

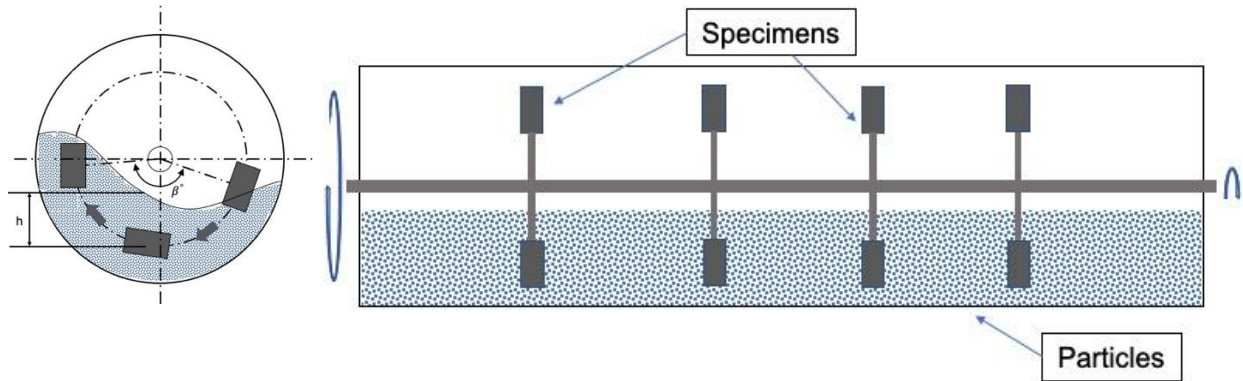


Figure 2: Schematic of the abrasion setup based on impeller tumbler method. The image on the left shows the movement of specimens through abrasive particles.

The unique design of the system allows for the setup to be operated inside a paragon dragon kiln maintained at temperatures >700 °C. The temperature distribution inside the kiln was verified using thermocouples to ensure that the particles and the test specimens reached a temperature of 800 °C before commencing the experiments. Two test setups were built for independent testing at room temperature and inside a kiln. The shaft can be loaded with up to 8 different specimens simultaneously and the relative velocity between the particles and the containment specimens is controlled by using a speed-controlled motor as well as the distance of the sample from the shaft at ~ 3.5 cm/s. To evaluate the role of surface oxidation in comparison to abrasion-erosion, control samples were suspended in the kiln near the erosion rig but not submerged in the particles. The depth of the particle bed is kept such that the specimens are completely submerged in the particle bed as they pass through particles. The actual test setup used for testing at 800 °C is shown in Figure 3.



Figure 3: Abrasion test setup for testing at 800 °C. Mounted in this image are SS316, Inconel 740H, and fireclay cement type refractory specimens running through a bed of HSP 40/70 particles.

The specimens are removed from the test setup periodically and measured for changes in mass. It is more typical to express corrosion in mg/cm^2 unit, as such, the mass changes in each specimen are subsequently divided by the surface area subject to abrasion wear as shown in equation (1):

$$W_{AO} = \frac{m_i - m_0}{A_S} \quad (1)$$

In the above equation, m_i is the mass of specimen at after i^{th} test, m_0 is the initial mass of specimen at time 0, and A_S is the total surface area of the specimen exposed to particles. The abrasion wear can subsequently be converted to specific wear rate (in $\text{mm}^3 \text{N}^{-1} \text{m}^{-1}$) as per equation (2) to account for the density differences between the materials tested (Antonov and Hussainova, 2009).

$$k = \frac{W_{AO}}{pv(\beta/360)\rho_M} 2778 \quad (2)$$

Where W_{AO} is the abrasion wear in mass change per unit surface area from a combination of abrasion and corrosion, p is the mean pressure of abrasive, v is the speed of specimen movement, β is the duration of the specimen's center immersion to the abrasive (in degrees), ρ_M is the density of specimen material, and 2778 is a correction factor for unit conversion. The pressure p of the abrasive is calculated from the particle bulk density ρ_A , packing fraction K_p , acceleration due to gravity g , and immersion depth h as follows:

$$p = h\rho_A K_p g \quad (3)$$

The properties of the materials tested as well as the other test conditions are provided in the Table 3 below:

Table 3: Test conditions and material mechanical properties

v	3.5 cm/s
β	132 degrees
$\rho_{M_Refractory}$	2.46 g/cm^3
ρ_{M_SS316}	7.95 g/cm^3
$\rho_{M_NickelAlloy}$	8.05 g/cm^3
h	1.7 cm
ρ_A	2.06 g/cm^3
K_p	0.62
g	9.8 m/s^2

2.3. Microstructure Analysis

Selected samples (both after erosion testing and control samples) were metallurgically examined. Prior to sample sectioning, non-contact surface area and line roughness measurements were performed on each sample side using a Keyence VR-3200 LED measuring microscope. For post-test destructive microstructural analysis, the metallic specimens were sectioned using a slow speed saw and mounted using conductive Bakelite in multiple orientations to allow for cross-sectional evaluation of the surfaces and oxide scales. Samples were polished using standard

metallographic techniques with a final polish of >20hours in a vibratory polisher to reveal oxide structure. Figure 4 illustrates the sample cut lines, nomenclature, and image orientations examined. Analysis of the metallic samples, oxide scale, and any remaining surface debris was conducted using optical metallography (Keyence VHX-7000) and scanning electron microscopy (SEM) using a FEI Teneo Field Emission Gun SEM in backscatter imaging (BSE) with semi-quantitative compositional analysis performed by Energy Dispersive Spectroscopy (EDS).

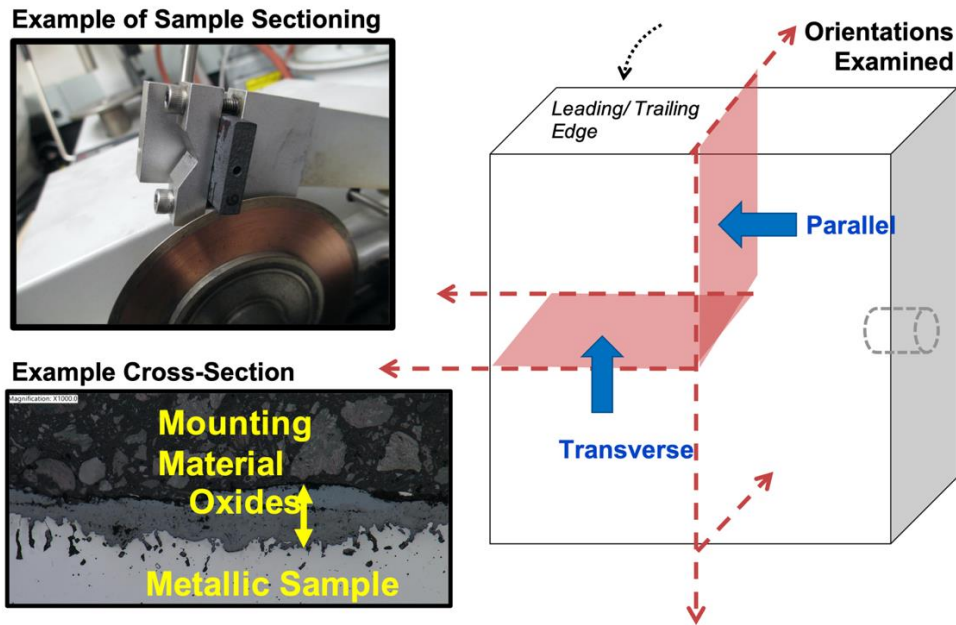


Figure 4: Illustration of planes along which the slow speed saw is used to prepare specimens for microstructural analysis.

3 Results

Tests were conducted at room temperature as well as 800 °C in order to determine the effects of temperature on abrasion wear. The individual observations are covered in the subsequent sections. In order to ensure repeatability, multiple specimens of the same material were loaded and the abrasion wear for each material type was observed to follow similar trends. The results presented below are from taking a mean of the abrasion wear on all specimens for each material type. The results for each individual specimen tested at room temperature and at 800 °C, are provided in the supplemental material.

3.1. Room Temperature Abrasion Test Results

The results from experiments at room temperature are shown in Figure 5. The plot shows the average abrasion wear (Refer equation (1)) for each material type with time. It is noted that for the refractory material, the abrasion wear increases more rapidly initially compared to the metallic specimens, eventually leveling out. This is attributed to the composite nature of the refractory material. Initially some of the softer, finer binder phases between the large grains may have been quickly worn away resulting in the sharper mass loss for the material. This could also explain a sudden spike observed in the early hours of testing as smaller abrasive particles get lodged in porous spaces in the test specimen. A more important observation from the experiments at room temperature was that the abrasion wear for both 316 and 740H specimens are near similar at low velocities. For these experiments, the specific wear rate was calculated after abrasion wear for the specimens reached a steady state value. For the 316, 740H, and the refractory material, specific wear rate at the end of the experiments were calculated to be $3.63\text{E-}5 \text{ mm}^3 \text{ N}^{-1} \text{ m}^{-1}$, $3.76\text{E-}5 \text{ mm}^3 \text{ N}^{-1} \text{ m}^{-1}$, and $3.53\text{E-}4 \text{ mm}^3 \text{ N}^{-1} \text{ m}^{-1}$ respectively. The value of specific wear rate for 316 obtained from these experiments was nearly an order lower than the previously reported range of $2.5\text{E-}4 \text{ mm}^3 \text{ N}^{-1} \text{ m}^{-1}$ and $1.9\text{E-}3 \text{ mm}^3 \text{ N}^{-1} \text{ m}^{-1}$ (Antonov and Hussainova, 2009). This could be attributed to the different abrasive particle used and differences in the test setup design.

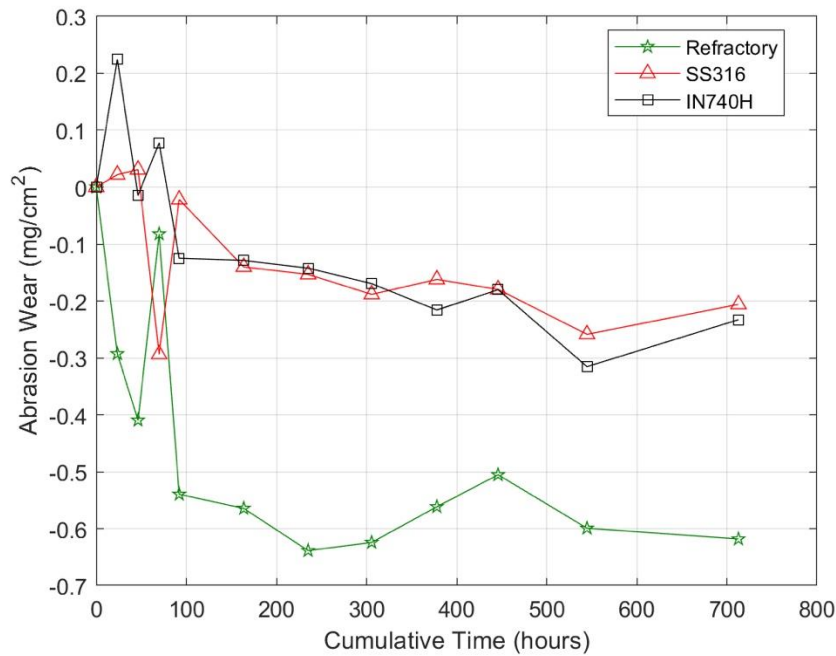


Figure 5: Abrasion erosion in 316, 740H, and refractory material from high alumina HSP 40/70 ceramic particles as room temperature. The experimental error in abrasion wear for SS316 and Inconel 740H were 32% and 5% respectively at the end of experiment, whereas that for the refractory material was 27%

3.2. 800 °C Temperature Abrasion

At 800 °C, the abrasion wear observed for the tested materials was significantly higher compared to that noted at room temperature. In the presence of atmospheric oxygen, the metallic specimens in particular developed a layer of oxide build over time which subsequently wore off under abrasive wear from the particles. Comparing the mass change in the oxidation control samples to the erosion samples suggests that erosion is significantly greater than the oxidation for the 316 but much less so than for the 740H. The results from the high temperature experiments are shown in Figure 6. From the results, an initial sharp change in abrasion wear was observed for the fireclay cement type refractory material specimens subject to abrasion. Subsequently, a second rapid decline in wear rate is observed after the initial break-in period. Given the ceramic composition of refractory materials, the losses from oxidation are expected to be minimal, however, the abrasion wear noted at 800 °C was nearly 50 times that observed at room temperature with a specific wear rate of $1.99\text{E-}2 \text{ mm}^3 \text{ N}^{-1} \text{ m}^{-1}$.

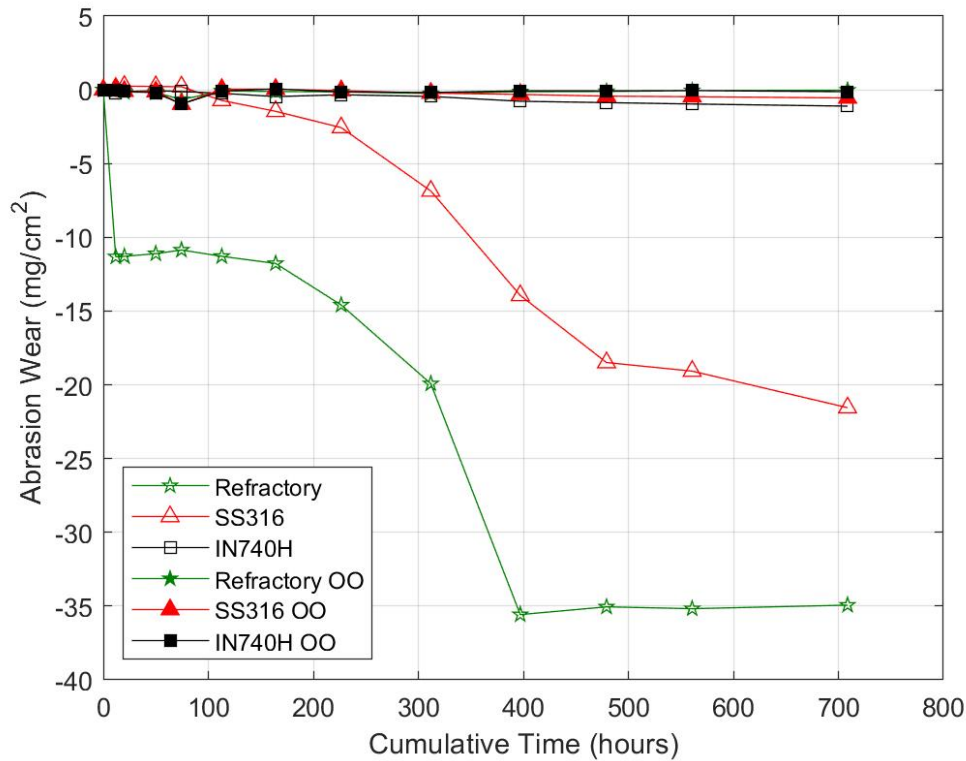


Figure 6: Abrasion erosion in refractory material, 316 and 740H from high alumina HSP 40/70 ceramic particles as 800 °C. Here suffix “OO” refers to control specimens that were exposed to oxidation only. The experimental error in abrasion wear for SS316 and Inconel 740H were 6% and 19% respectively at the end of experiment, whereas that for the refractory material was 4%

Between the two metallic specimens, abrasion wear at 800 °C in 316 and 740H specimens no longer exhibited similar trends. While the abrasion wear in 316 specimens was nearly 3 orders of magnitude higher than the experiments at room temperature, 740H specimens exhibited extremely low abrasion wear, following near similar trend as that observed in the 740H control specimen. At the end of experiment, the specific wear rate of 316 and 740H specimens were calculated to be $3.9\text{E-}3 \text{ mm}^3 \text{ N}^{-1} \text{ m}^{-1}$ and $2.17\text{E-}4 \text{ mm}^3 \text{ N}^{-1} \text{ m}^{-1}$ respectively. However, inspection of the 316 data suggest the calculated average rates may be conservative as there is clear transition in rate after ~400 hours where the erosion rate slows. This complex transitory behavior and observed difference in resistance to abrasion wear between the two metallic specimens may be attributed to the morphology of oxide layers formed on two materials. To elucidate the potential combined effects of oxidation and abrasion-wear, microstructure analysis was performed on the metallic erosion samples and control samples after testing at 800 °C for 709 hours. The results from abrasion experiments at room temperature and at 800 °C are summarized in Table 4:

Table 4: Abrasion wear and Specific Wear from experiments at room temperature and at 800 °C after 709 hours of testing

	Room Temperature		800 °C	
	Abrasion Wear (mg cm ⁻²)	Specific Wear Rate (mm ³ N ⁻¹ m ⁻¹)	Abrasion Wear (mg cm ⁻²)	Specific Wear Rate (mm ³ N ⁻¹ m ⁻¹)
SS 316	0.2060	3.63E-05	21.9832	3.90E-03
Inconel 740H	0.2158	3.76E-05	1.2366	2.17E-04
Refractory	0.6199	3.53E-04	34.7444	1.99E-02

3.3. Microstructural Analysis (Metallic Samples)

Figure 7 shows a composite optical microscopy image of the different erosion sample orientations for both metallic materials after testing and the control samples. The 316 samples all showed much thicker duplex oxides and evidence of possible oxide scale spallation or erosion in comparison to the 740H which formed a relatively thin uniform dense oxide scale. Figure 8 shows the entire leading/trailing edge of the 316 erosion sample. Some rounding of the sample corners was observed along with highly irregular thickness in the oxide scale. Similar analysis of the 740H did not show as pronounced rounding indicating some of the mass loss may be more localized to sample corners in the 316. However, there was some sample-to-sample variation in corner and surface preparation which was not fully characterized prior to testing. Further investigation using LED microscope surface imaging and topological measurements did not show large differences in surface roughness from sample to sample indicating a generally macroscopic uniform wear. Thus, the overall impact of sample edge geometry appears to be minimal for this experimental set-up condition.

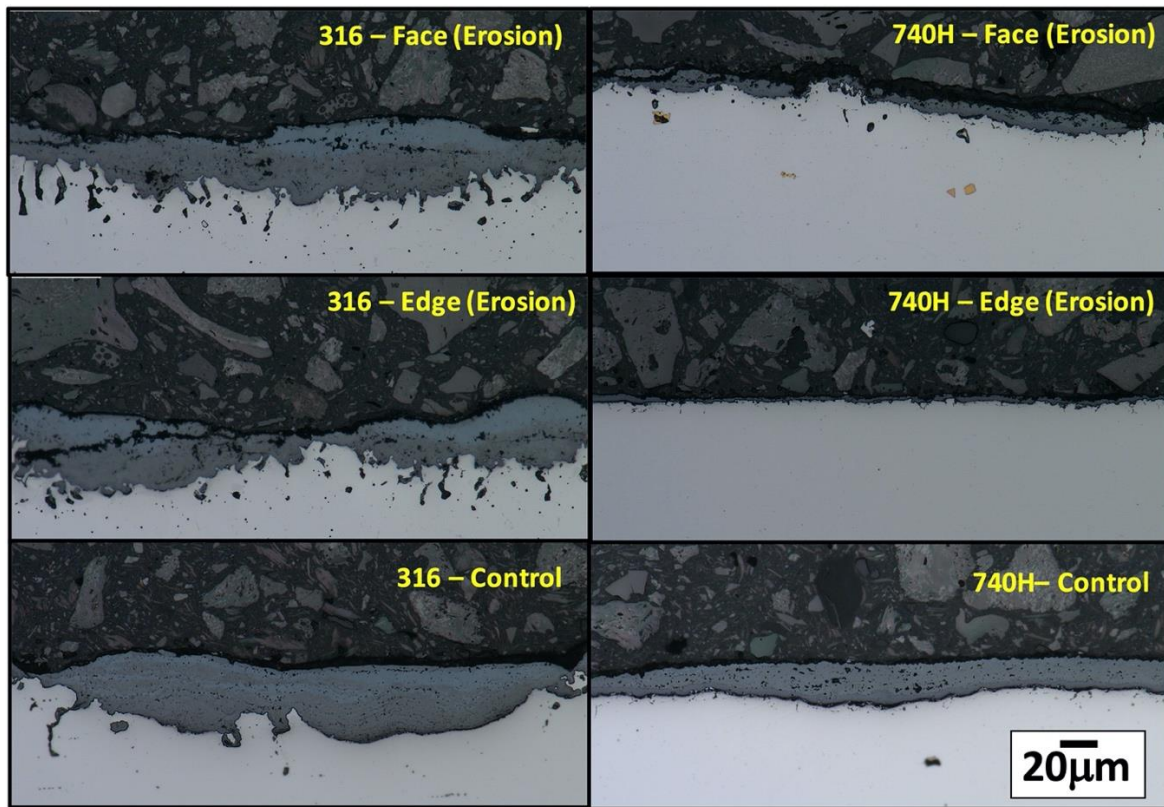


Figure 7: Optical images of oxide scales on different faces of the erosion samples and the control samples for 316 and 740H

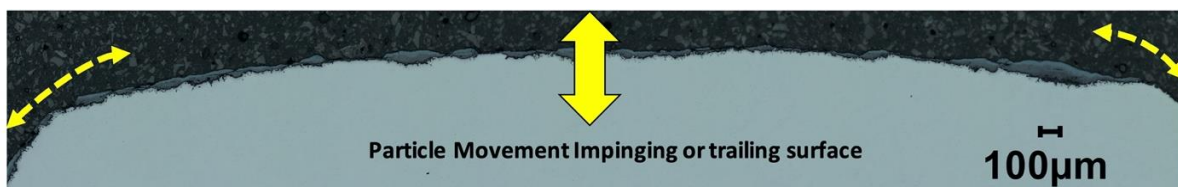


Figure 8: Stitched optical image of the 316 leading/trailing edge showing rounding of sample corners and irregular nature of the oxide scale at the microscopic level

To examine the specific nature of the oxide scales in more detail, regions of exfoliation and oxide scale adhesion were examined. Figure 9 shows the elemental distribution for the 316 sample in a region where significant loss of the outer oxide scale was observed. The BSE image shows a rough surface and a tortuous inner oxide layer. An enrichment in chromium below the outer oxide with an Fe-Cr spinel was confirmed with EDS. Careful examination of what appeared to be a roughened surface or lightly adherent particles show these to be of a Fe-Ni-Cr oxide indicating that erosion of the oxide scale occurred during the testing. No evidence of adhered or imbedded erodent was identified. The dense chromia scale formed appeared to be stable and at this location protected by the outer oxide which was eroding. This suggests a stable long-term oxidation protection in this region for these conditions after erosion of the outer iron oxide and slowed growth and erosion of the inner Fe-Cr spinel. This may be reflected in the change in slope (reduced rate) after ~400h of testing reported in Figure 6.

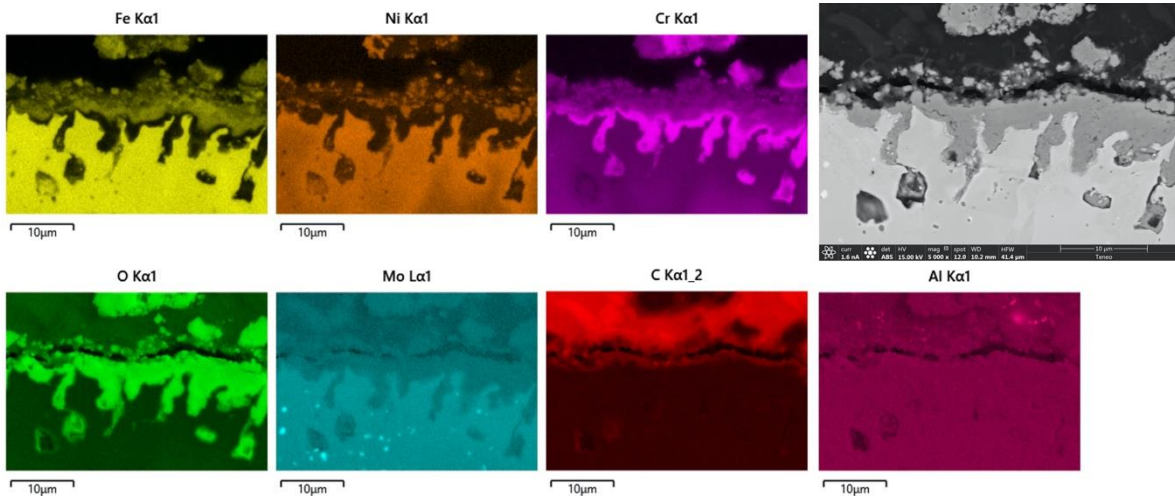


Figure 9: BSE (upper right) and elemental EDS maps for an exfoliated region of the 316 sample.

Figure 10 shows a similar image to Figure 9 but for the 740H sample after erosion testing. A dense Chromia scale (Cr_2O_3 type) a few microns in thickness extends across the entire sample; little evidence was found for any erosion product of the chromia scale. Occasional internal oxidation of the Titanium and Aluminum was observed along grain boundaries but does not appear to be affected by erosion.

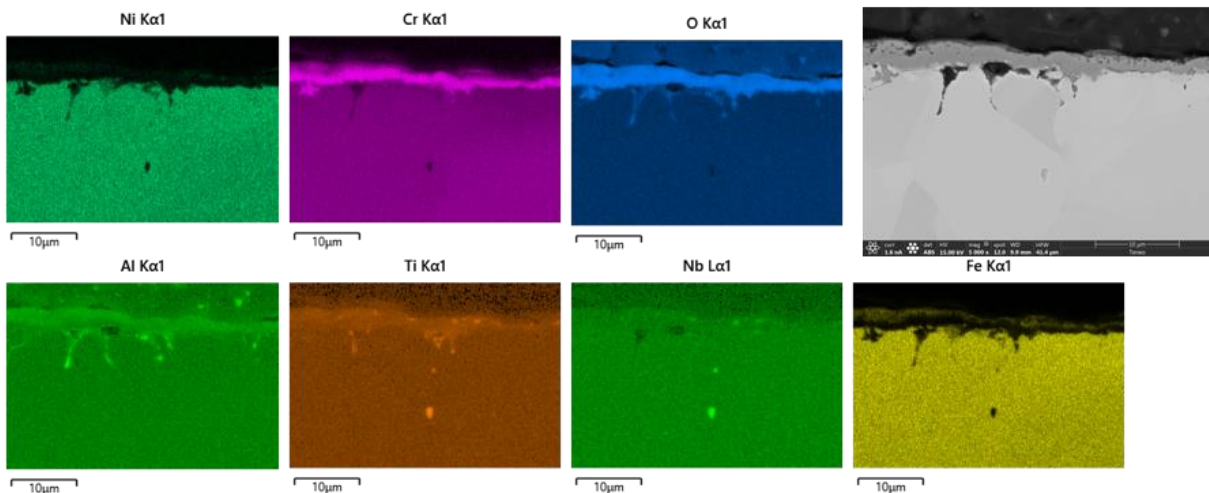


Figure 10: BSE (upper right) and elemental EDS maps for a typical region in the 740H sample

4 Discussion

Erosion and abrasion of metallic materials at high temperature can be a challenging phenomenon to properly model and understand (Sundararajan and Manish, 1997; Wright, 2001). In comparison to the recent work of Galiullin et al (Galiullin et al., 2019), the erosion-wear rates were much lower (and likely realistic for CSP receivers) in this work. As such, in their work the damage mechanism would likely be described as pure metal erosion or oxidation effected erosion where the formation of the oxide scale had minimal impact on the measured wear or erosion rates. Their measured rates for a martensitic steel, nickel-based alloy, and stainless steel were all similar.

In contrast for this work, based on the limited but repeatable data at 800 °C for times >500 hours and supported by the microscopy, the most plausible mechanism for surface degradation (based on Sundararajan & Roy's classification) was 'Oxidation Controlled Erosion (Continuous)'. In this mechanism, the oxidation of the metal plays a critical role in determining the overall metal loss due to erosion. This was clearly evident in the mass loss data when comparing the 316 to the 740H and each metal individually to the control samples. Figure 11 attempts to summarize the complex situation which occurred and why the 316 showed such as significant mass loss in comparison to the 740H. For the 316, a duplex oxide with an inner spinel and outer iron oxide initially formed and grew. This thermally grown oxidation process has been described and characterized in detail by researchers and is summarized using long-term field observations in boiler tubing (EPRI, 2015). Somewhat surprisingly, few oxidation studies have been conducted on alloy 316 in air at the specific temperature of 800 °C, but the available data shows a small mass gain is generally associated with this process (Buscail et al., 2011). In 300 series stainless steels, the morphology of the oxide scale is controlled by the diffusion rates of Fe and Cr to the alloy surface and the diffusion of oxygen through the oxide scale into the surface. Grain size, surface condition (such as cold work), and specific concentration of elements such as Cr (even within the specification) are known to dramatically change the oxide scale morphology. The observed scale in Figure 7 is very typical in long-term high-temperature oxidation of 300 series stainless steels.

Similar to oxidation of stainless steels in steam (Sabau et al., 2012), as this duplex oxide scale grew, defects originated at the interface between the two oxide layers eventually leading to loss (exfoliation) of the outer layer. However, in these erosion experiments, it appeared that the erosion process was able to remove portions of the entire oxide (both layers) which is seen in both the SEM analysis of the erosion products on the sample surface (they are oxides not the erodent) and in the optical images where the entire oxide scale has been removed. This exposed the internally oxidized zone where some regions may be protective (due to chromia formation such as in Figure 9) or where local composition allowed for re-growth of the oxide (see Figure 11). This happened continuously which explains the slow mass loss (oxide formation), followed by rapid mass loss (erosion of the oxide), and slower but continuous mass loss (erosion-oxide growth-erosion-oxide growth) as seen in Figure 6 after ~400hours.

In contrast, the mass loss of the 740H was higher than the oxidation alone mass loss ("OO" sample), but it showed no change in slope and was minor in comparison to the 316. This suggests that there may be a small continuous erosion of the stable chromia scale but no major separation of the oxide scale and the underlying base metal. It is well established that the slower diffusion of Ni and high Chromium content of these nickel-based alloys promote a dense chromia scale in comparison to iron-based alloys.

From a long-term perspective, longer tests at multiple temperatures would be valuable to understanding and modeling this phenomenon. In particular, once all the duplex outer oxide has been eroded and exfoliated from the 316, the stability of the internal chromia scale should support a lower mass loss (which is suggested by the change in rate after ~400hours), but the rate of loss will likely be highly affected by variables such as operational temperature and alloying elements which effect diffusion of Chromium to the alloy surface. Additionally, the role of surface roughness, as evidenced by the rounding of the specimen corners, should also be explored. The use of stainless steels is desired due to wide availability and lower cost in comparison to nickel-based alloys. This opens up the opportunity for exploring ways to improve long-term performance. While coatings could be utilized, this may add significant cost and the size and geometry of the components would need to be considered. One alternative opportunity for surface enhancement in the alloy 316 may be the use of shot-peening which have been shown to greatly improve oxidation resistance of some stainless steels at high temperature (Kurley and Pint, 2020). This has been demonstrated as a highly effective measure applicable to large scale powerplant applications globally for relatively low-cost (EPRI, 2014). If the mechanism is oxidation dominated (i.e. oxidation-controlled erosion), then slight improvements in oxidation resistance may allow for the use of less alloyed materials such as 300 series stainless steel instead of nickel-based alloys.

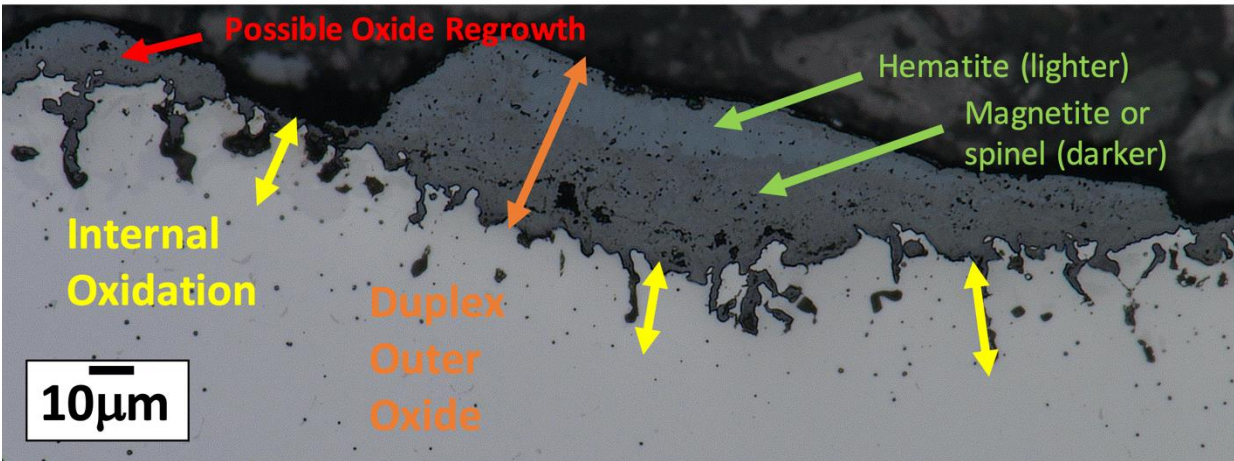


Figure 11: Summary of observed characteristics for observations in the 316 sample

5 Conclusions

A bespoke erosion experiment was performed on multiple materials including two metallics and one refractory to simulate conditions in a falling particle CSP receiver. While the metallic specimens showed little to no wear from abrasion at room temperature, the wear in refractory material was nearly three times higher than those noted for the metallic specimens. However, experiments at 800 °C indicated an increase in wear rate of metallic specimens by an order of magnitude or higher. Detailed analysis of 316 stainless steel and nickel-based alloy 740H after 709 hours of testing at 800 °C, showed that for the conditions tested oxidation-controlled erosion was the likely mechanism occurring at the sample surfaces. This translated into a rapid mass loss in the 316 sample as the thick duplex oxide layer was eroded over time. In contrast, the dense adherent chrome oxide scale showed very little erosion for the 740H making it a good candidate for long lifetime at these conditions.

In summary, it was noted that even at the low mass flow rates studied in this work, degradation in material from wear is possible and even enhanced at high temperatures due to formation of oxides. Future work to extend testing times, explore additional temperatures, additional materials with a range of mass fraction of different comprising elements and evaluate the use of surface modifications for improved performance could all provide benefit to improved modeling and practical application of this new technology.

Declaration of Competing Interest

The authors declare no conflicts of interest.

Acknowledgements

The authors would like to acknowledge support from the U.S. Department of Energy Solar Energy Technologies Office under award number DE-EE0008370 and one author (JPS) acknowledges the support from the U.S. Department of Energy Solar Energy Technologies Office under award number 34211. The authors would also like to thank Sandia National Labs for guidance and fruitful discussion over the course of this work. The authors would like to thank Stephen Tate and Mary K. Havens (EPRI) for their assistance with metallographic preparation and analysis.

References

- Antonov, M., Hussainova, I., 2009. Experimental setup for testing and mapping of high temperature abrasion and oxidation synergy. *Wear* 267, 1798–1803. <https://doi.org/10.1016/j.wear.2009.01.008>
- Arabnejad, H., Shirazi, S.A., McLaury, B.S., Subramani, H.J., Rhyne, L.D., 2015. The effect of erodent particle hardness on the erosion of stainless steel. *Wear* 332–333, 1098–1103. <https://doi.org/10.1016/j.wear.2015.01.017>
- Bai, F., Zhang, Y., Zhang, X., Wang, F., Wang, Y., Wang, Z., 2014. Thermal Performance of a Quartz Tube Solid Particle Air Receiver. *Energy Procedia* 49, 284–294. <https://doi.org/10.1016/j.egypro.2014.03.031>
- Buscail, H., El Messki, S., Riffard, F., Perrier, S., Issartel, C., 2011. Effect of pre-oxidation at 800 °c on the pitting corrosion resistance of the AISI 316L stainless steel. *Oxid. Met.* 75, 27–39. <https://doi.org/10.1007/s11085-010-9218-2>
- El-Leathy, A., Jeter, S., Al-Ansary, H., Abdel-Khalik, S., Roop, J., Golob, M., Danish, S., Alrished, A., Djajadiwinata, E., Al-Suhaibani, Z., 2014. Thermal Performance Evaluation of Two Thermal Energy Storage Tank Design Concepts for Use with a Solid Particle Receiver-Based Solar Power Tower. *Energies* 7, 8201–8216. <https://doi.org/10.3390/en7128201>
- EPRI, 2015. Atlas of Steam-Side Oxide Scales Formed on Superheater and Reheater Tubes. Palo Alto, CA.
- EPRI, 2014. AEP Mitigates Risk of Exfoliation Damage in its Fleet. Palo Alto, CA.
- Finnie, I., 1960. Erosion of Surfaces By Solid Particles. *Wear* 87–103.
- Finnie, I., McFadden, D.H., 1978. On the velocity dependence of the erosion of ductile metals by solid particles at low angles of incidence. *Wear* 48, 181–190. [https://doi.org/10.1016/0043-1648\(78\)90147-3](https://doi.org/10.1016/0043-1648(78)90147-3)
- Flamant, G., 1982. Theoretical and experimental study of radiant heat transfer in a solar fluidized-bed receiver. *AIChE J.* 28, 529–535. <https://doi.org/10.1002/aic.690280402>
- Flamant, G., Gauthier, D., Benoit, H., Sans, J.-L., Garcia, R., Boissière, B., Ansart, R., Hemati, M., 2013. Dense suspension of solid particles as a new heat transfer fluid for concentrated solar thermal plants: On-sun proof of concept. *Chem. Eng. Sci.* 102, 567–576. <https://doi.org/10.1016/j.ces.2013.08.051>
- Galiullin, T., Gobreit, B., Naumenko, D., Buck, R., Amsbeck, L., Neises-von Puttkamer, M., Quadackers, W.J.J., 2019. High temperature oxidation and erosion of candidate materials for particle receivers of concentrated solar power tower systems. *Sol. Energy* 188, 883–889. <https://doi.org/10.1016/j.solener.2019.06.057>
- Ho, C.K., 2017. Advances in central receivers for concentrating solar applications. *Sol. Energy* 152, 38–56. <https://doi.org/10.1016/j.solener.2017.03.048>
- Ho, C.K., 2016. A review of high-temperature particle receivers for concentrating solar power. *Appl. Therm. Eng.* 109, 958–969. <https://doi.org/10.1016/j.applthermaleng.2016.04.103>
- Ho, C.K., Christian, J.M., E. Yellowhair, J., Armijo, K., Kolb, W.J., Jeter, S., Golob, M., Nguyen, C., 2019. On-Sun Performance Evaluation of Alternative High-Temperature Falling Particle Receiver Designs. *J. Sol. Energy Eng.* 141. <https://doi.org/10.1115/1.4041100>
- Ho, C.K., Christian, J.M., Yellowhair, J., Armijo, K., Kolb, W.J., Jeter, S., Golob, M., Nguyen, C., 2016. Performance Evaluation of a High-Temperature Falling Particle Receiver. <https://doi.org/10.1115/ES2016-59238>
- Hutchings, I., Shipway, P., Hutchings, I., Shipway, P., 2017. Wear by hard particles. *Tribology* 165–236. <https://doi.org/10.1016/B978-0-08-100910-9.00006-4>
- Kurley, J.M., Pint, B.A., 2020. The Effect of Shot Peening on Steam Oxidation of 304H Stainless Steel. *Oxid. Met.* 93, 159–174. <https://doi.org/10.1007/s11085-019-09951-9>
- Ma, Z., Glatzmaier, G., Mehos, M., 2014. Fluidized Bed Technology for Concentrating Solar Power With Thermal Energy Storage. *J. Sol. Energy Eng.* 136. <https://doi.org/10.1115/1.4027262>
- Martinek, J., Ma, Z., 2015. Granular Flow and Heat-Transfer Study in a Near-Blackbody Enclosed Particle Receiver. *J. Sol. Energy Eng.* 137. <https://doi.org/10.1115/1.4030970>
- Mehos, M., Turchi, C., Vidal, J., Wagner, M., Ma, Z., Ho, C., Kolb, W., Andraka, C., Kruiuzenga, A., 2017. Concentrating Solar Power Gen3 Demonstration Roadmap. Golden, CO (United States). <https://doi.org/10.2172/1338899>
- Misra, A., Finnie, I., 1981. On the size effect in abrasive and erosive wear. *Wear* 65, 359–373. [https://doi.org/10.1016/0043-1648\(81\)90062-4](https://doi.org/10.1016/0043-1648(81)90062-4)
- Oka, Y.I., Matsumura, M., Kawabata, T., 1993. Relationship between surface hardness and erosion damage caused by solid particle impact. *Wear* 162–164, 688–695. [https://doi.org/10.1016/0043-1648\(93\)90067-V](https://doi.org/10.1016/0043-1648(93)90067-V)

- Oka, Y.I., Okamura, K., Yoshida, T., 2005. Practical estimation of erosion damage caused by solid particle impact: Part 1: Effects of impact parameters on a predictive equation. *Wear* 259, 95–101. <https://doi.org/https://doi.org/10.1016/j.wear.2005.01.039>
- Sabau, A.S., Wright, I.G., Shingledecker, J.P., 2012. Oxide scale exfoliation and regrowth in TP347H superheater tubes. *Mater. Corros.* 63, 896–908. <https://doi.org/10.1002/maco.201206640>
- Sheldon, G.L., 1977. Effects of surface hardness and other material properties on erosive wear of metals by solid particles. *J. Eng. Mater. Technol. Trans. ASME* 99, 133–137. <https://doi.org/10.1115/1.3443422>
- Siegel, N.P., Gross, M.D., Coury, R., 2015. The development of direct absorption and storage media for falling particle solar central receivers. *J. Sol. Energy Eng. Trans. ASME* 137. <https://doi.org/10.1115/1.4030069>
- Siegel, N.P., Ho, C.K., Khalsa, S.S., Kolb, G.J., 2010. Development and Evaluation of a Prototype Solid Particle Receiver: On-Sun Testing and Model Validation. *J. Sol. Energy Eng.* 132. <https://doi.org/10.1115/1.4001146>
- Sundararajan, G., Manish, R., 1997. Solid particle erosion behaviour of metallic materials at room and elevated temperatures. *Tribol. Int.* 30, 339–359. [https://doi.org/10.1016/S0301-679X\(96\)00064-3](https://doi.org/10.1016/S0301-679X(96)00064-3)
- Wright, I.G., 2001. Is there any reason to continue research efforts on erosion-corrosion, in: *Proc. John Stringer Symposium on High Temperature Corrosion*. pp. 107–121.
- Wu, W., Amsbeck, L., Buck, R., Waibel, N., Langner, P., Pitz-Paal, R., 2014. On the influence of rotation on thermal convection in a rotating cavity for solar receiver applications. *Appl. Therm. Eng.* 70, 694–704. <https://doi.org/10.1016/J.APPLTHERMALENG.2014.03.059>
- Wu, W., Trebing, D., Amsbeck, L., Buck, R., Pitz-Paal, R., 2015. Prototype Testing of a Centrifugal Particle Receiver for High-Temperature Concentrating Solar Applications. *J. Sol. Energy Eng.* 137. <https://doi.org/10.1115/1.4030657>